

First-principles calculations of stability, optical properties, and non-radiative hole capture rates of carbon defects in wurtzite AlGaN alloys

Qian-Ji Wang(王千觊), Hao-Rui He(贺浩锐), Fang-Jing Kang(康芳静), Ze Peng(彭泽), Lin Shi(石林), Shao-Qiang Guo(郭少强), Juan Lyu(吕娟), Hai-Shan Zhang(张海山), and Jian Gong(宫箭)
Citation: Chin. Phys. B, 2026, 35 (**8**): 087701. DOI: 10.1088/1674-1056/ae156a
http://cpb.iphy.ac.cn; http://iopscience.iop.org/cpb

What follows is a list of articles you may be interested in

Sliding ferroelectricity and tunable linear and nonlinear optical properties in bilayer SnP_2Se_6

Huicong Li(李汇聪), Yali Yang(杨亚利), Jiangang He(和建刚), and Rongming Wang(王荣明)
Chin. Phys. B, 2026, 35 (**7**): 077702. DOI: 10.1088/1674-1056/ae8441

Effective strategy of enhancing piezoelectricity in stable $CrSiN_4Sn$ semiconductor monolayers by atom-layer-pair effect

Qi-Wen He(贺绮雯), Dan-Yang Zhu(朱丹阳), Jun-Hui Wang(王俊辉), He-Na Zhang(张贺娜), Xiao Shang(尚骁), Shou-Xin Cui(崔守鑫), and Xiao-Chun Wang(王晓春)
Chin. Phys. B, 2025, 34 (**5**): 057701. DOI: 10.1088/1674-1056/adb7d1

Multiferroic monolayers VO*X* (*X* = Cl, Br, I): Tunable ferromagnetism via charge doping and ferroelastic switching

Hong-Chao Yang(杨洪超), Peng-Cheng Liu(刘鹏程), Liu-Yu Mu(穆鎏羽), Ying-De Li(李英德), Kai Han(韩锴), and Xiao-Le Qiu(邱潇乐)
Chin. Phys. B, 2023, 32 (**6**): 067701. DOI: 10.1088/1674-1056/acaa2b

Strain-modulated ultrafast magneto-optic dynamics of graphene nanoflakes decorated with transition-metal atoms

Yiming Zhang(张一鸣), Jing Liu(刘景), Chun Li(李春), Wei Jin(金蔚), Georgios Lefkidis, and Wolfgang Hübner
Chin. Phys. B, 2021, 30 (**9**): 097702. DOI: 10.1088/1674-1056/abeef1

First-principles calculation of influences of La-doping on electronic structures of KNN lead-free ceramics

Ting Wang(王挺), Yan-Chen Fan(樊晏辰), Jie Xing(邢洁), Ze Xu(徐泽), Geng Li(李庚), Ke Wang(王轲), Jia-Gang Wu(吴家刚), Jian-Guo Zhu(朱建国)
Chin. Phys. B, 2020, 29 (**6**): 067702. DOI: 10.1088/1674-1056/ab84db

---

First-principles calculations of stability, optical properties, and non-radiative hole capture rates of carbon defects in wurtzite AlGaN alloys

Qian-Ji Wang(王千觊)[1,2], Hao-Rui He(贺浩锐)[3], Fang-Jing Kang(康芳静)[1], Ze Peng(彭泽)[1], Lin Shi(石林)[4], Shao-Qiang Guo(郭少强)[1], Juan Lyu(吕娟)[1], Hai-Shan Zhang(张海山)[1,†], and Jian Gong(宫箭)[1,5,6,‡]

[1] *School of Physical Science and Technology, Inner Mongolia University, Hohhot* 010021, *China*
[2] *Ganjiang Innovation Academy, Chinese Academy of Sciences, Ganzhou* 341100, *China*
[3] *Inner Mongolia Aerospace Hong Gang Machinery Corporation Limited, Hohhot* 010076, *China*
[4] *Department of Physics, Yancheng Institute of Technology, Yancheng* 224051, *China*
[5] *College of Physics and Electronic Information, Inner Mongolia Normal University, Hohhot* 010021, *China*
[6] *Ordos Institute of Technology, Ordos* 017000, *China*

(Received 14 August 2025; revised manuscript received 7 October 2025; accepted manuscript online 21 October 2025)

AlGaN alloy has a wide range of applications in ultraviolet photodetectors. Carbon defects, though detrimental as carrier capture centers, offer a tunable pathway for defect-mediated optoelectronic engineering in AlGaN alloys. By combining first-principles calculations with configurational sampling, we systematically resolve the thermodynamic stability of $Al_xGa_{1-x}N$ ($x = 0.33$, 0.50, 0.61) alloy, and determine that the carbon atom will occupy the nitrogen point position. Taking into account *c*-axis polarity of wurtzite structure and carbon-on-nitrogen substitutional defect (C_N) nearest neighbor atomic arrangement, the eight possible configurations are constructed, and the polarity has little effect on the total energy (ΔE is 0.02 eV–0.07 eV). After ignoring the *c*-axis polarity, the formation energy of 8 possible C_N defect configurations increases linearly with the number of Al neighbors ($n = 0$, 1, 2, 3, 4, meaning the number of Ga neighbors is 4, 3, 2, 1, 0), and the influence of different configurations on the transition level is less than 0.2 eV. Because the formation energy difference of five configurations is less than 1.22 eV, all these defect configurations may appear in the actual growth process of AlGaN alloy. In addition, the calculation results of the optical transition process show that the photoabsorption (PA) and photoluminescence (PL) energies are also linear with the Al contents. For the non-radiative recombination process of defect transition levels, since the 5 possible configurations produce a transition level fluctuation within 0.18 eV, each 0.1-eV energy fluctuation corresponds to an order of magnitude in the hole capture cross-section fluctuation. Strategic Al content modulation enables precise tuning of defect transition levels, offering a direct route to suppress non-radiative recombination in ultraviolet (UV) photodetectors.

Keywords: AlGaN alloy, point defect, non-radiative recombination, capture cross-section, first-principles calculation

PACS: 77.84.Bw, 61.72.J–, 78.60.–b, 63.20.dk

DOI: 10.1088/1674-1056/ae156a **CSTR:** 32038.14.CPB.ae156a

1. Introduction

III–nitride semiconductor materials such as GaN, AlN, and AlGaN ternary alloys have great potential in ultraviolet (UV) optoelectronics or high-frequency and high-power diode electronics.[1–4] In the preparation of III–nitride materials by metal organic chemical vapor deposition (MOCVD) method, the deep defect transition level introduced by C defects usually acts as the non-radiative recombination center, which reduces the performance of AlGaN photoelectric devices. Photoluminescence (PL) spectroscopy is a nondestructive characterization technique compared with secondary ion mass spectrometry (SIMS) and can be used for conventional, nondestructive defect identification. And it has been experimentally confirmed that C defects cause intense photoabsorption (PA) with energies above 0.7 E_g in $Al_xGa_{1-x}N$ ($0 \le x \le 1$) materials accompanied by bright PL.[5–10] When the concentration of C defects increases to 2×10^{16} cm^{-3}, the non-radiative recombination center will be generated, which reduces the quantum efficiency.[10–12] Accurate identification of defect centers in AlGaN alloy materials and in-depth study of defect-related photoelectric properties can promote the efficient application of AlGaN-based devices in various fields. However, it is difficult to identify the microscopic source of the defect center experimentally because of the different sensitivities of the defect transition level to the cation concentration, band gap, band edge, and metal cation distribution in the alloy.

†Corresponding author. E-mail: hszhang@imu.edu.cn
‡Corresponding author. E-mail: ndgong@imu.edu.cn

© 2026 Chinese Physical Society and IOP Publishing Ltd. All rights, including for text and data mining, AI training, and similar technologies, are reserved.

In terms of theoretical investigations, current research on defect centers in alloy materials predominantly focuses on calculating transition levels, luminescence peak positions, zero-phonon lines, and related parameters,[13–15] while largely neglecting the carrier non-radiative recombination processes within defect centers. Density functional theory (DFT) calculations have been employed to study the photoelectric properties of C-doped GaN and AlN pure-phase systems. It is shown that C defects preferentially occupy nitrogen sites (where C_N^- constitutes the dominant defect state in n-type samples) rather than cation or interstitial sites.[16–18] The PL energy associated with the C_N $(0/-)$ transition level in AlGaN is predicted to a range from 2.2 eV (GaN) to 3.9 eV (AlN).[19–23] Although extensive theoretical efforts have been devoted to understanding the photoelectric characteristics of C_N defects in pure compounds, significant challenges persist in extrapolating these findings to ternary or quaternary alloy systems. Furthermore, the correlation between the photoelectric behavior of AlGaN alloys with varying defect configurations and their aluminum content remains poorly understood.

Experimentally, Rigutti *et al*. have verified the random distribution of cations in InGaN alloy by atom probe tomography (APT) technology.[24] In alloy materials, the physical properties of point defects exhibit significant variations depending on the spatial distribution of neighboring atoms surrounding defect sites. Wickramaratne *et al*. systematically constructed twelve distinct V_{Ga}–X and C_N atomic configurations within InGaN supercells, revealing transition level fluctuations spanning 0.32 eV.[13] Given that the relative positioning of defect transition levels within the bandgap fundamentally governs both defect-mediated optical transitions[25,26] and carrier recombination processes between defect centers and band edges,[27–29] the experimentally observed photoelectric phenomena associated with point defects in alloys should be interpreted as statistical manifestations of multiple coexisting atomic configurations.

In this work, through first-principles calculations of formation energies, we unequivocally resolve the preferential nitrogen-site occupancy of C_N defect in AlGaN alloys. By comprehensively modeling all eight possible defect configurations, accounting for wurtzite c-axis polarity and nearest-neighbor atomic environments, we demonstrate that local atomic arrangements induce remarkably small transition level variations (< 0.2 eV) at fixed Al compositions. Crucially, we establish two fundamental relationships: (i) a linear scaling law between optical transition energies and Al concentration, and (ii) a logarithmic correlation where each 0.1-eV shift in defect transition level alters hole capture cross-sections by an order of magnitude. These quantitative principles not only provide a predictive framework for defect spectroscopy in III–nitride alloys but also enable targeted defect engineering through Al composition tuning, a strategy directly applicable to UV photodetector optimization.

2. Calculation details

The first-principles calculations are based on DFT using the hybrid functional of Heyd–Scuseria–Ernzerhof (HSE)[30,31] as implemented in the PWmat software.[32,33] The mixing parameter (α) for the Hartree–Fock potential is taken as 0.31. To ensure the reliability of the conclusion regarding the stability of the doping configuration, we systematically tested the convergence of the formation energy with the same C_N defect nearest-neighbor atomic arrangement for $2\times2\times1$, $3\times3\times2$, and $4\times4\times2$ supercell sizes (as shown in Fig. S1 of supporting information). It was found that the formation energy of C_N defect had fully converged in the $3\times3\times2$ supercell, and the difference with the results of the $4\times4\times2$ size was only 0.003 eV, which was negligible. Therefore, the $4\times4\times2$ supercell of 128-atoms adopted in this paper can effectively eliminate the size effect. To ensure that the 128-atom supercell model adopted in this study can accurately fold the band edges to the Gamma point, thereby guaranteeing the reliability of subsequent electronic structure and electron–phonon coupling calculations, we conducted a rigorous verification of it. First, we calculated the complete band structure of the original unit cell as a benchmark. Subsequently, we obtained the equivalent band structure of the undoped 128-atom supercell using the band expansion technique. Figure S2 demonstrates that the expanded supercell bands exhibit excellent consistency with the original unit cell bands, particularly near the band edges at the Gamma point, thereby confirming the supercell's reliability. In $Al_xGa_{1-x}N$ alloy, the process of randomly replacing aluminum atoms in the cation lattice was simulated using statistical methods. For a given target composition ($e.g.$, $x = 0.5$), we started from a perfect GaN crystal-type gallium–nitride supercell (a $4\times4\times2$ supercell with 128 atoms). We used a Python script to randomly select and replace 32 Ga atoms with Al atoms to ensure the required chemical composition. This approach is conceptually consistent with the goal of the special quasi-random structure (SQS) method,[34] which is to create a computational model capable of capturing the basic disorder of random alloys. To ensure the statistical reliability of our results, we generated multiple independent random structures for each alloy composition. Through simple relaxation, we found that the arrangement of atoms had a negligible impact on the total energy of the system under the same atomic ratio. Therefore, we selected one configuration for each component to subsequent calculations. All C related defect calculations were performed with the summations over the Brillouin zone were approximated by one k point (Γ), a plane-wave basis set with a cutoff of 70 Ry and force optimization accuracy was set at 0.02 eV/Å. The calculated lattice parameters for GaN are

$a = b = 3.16$ Å and $c = 5.14$ Å, and for AlN are $a = b = 3.10$ Å and $c = 4.96$ Å, and the bandgaps of $Al_xGa_{1-x}N$ ($0 \le x \le 1$) varies from 3.52 eV of GaN to 6.03 eV of AlN with the change of Al contents, which is consistent with the experiment.[35,36]

3. Results and discussion

3.1. Stable region in chemical potential spaces and defect formation energies

The defect formation energy of C-doped AlGaN alloys depends on the atomic chemical potential, which is thermodynamically limited by several conditions. First, taking $Al_{0.33}Ga_{0.67}N$ as an example, the chemical potential must be smaller than its corresponding solid element to avoid the precipitation of Al, Ga, and N:

$$\Delta\mu_{Al} \le 0, \quad \Delta\mu_{Ga} \le 0, \quad \Delta\mu_{N} \le 0. \tag{1}$$

At the same time, to ensure the formation of thermodynamically stable $Al_{0.33}Ga_{0.67}N$ compounds, the chemical potential must satisfy the following equation:

$$0.33\Delta\mu_{Al} + 0.67\Delta\mu_{Ga} + \Delta\mu_{N} = \Delta H_f\left(Al_{0.33}Ga_{0.67}N\right). \tag{2}$$

Second, other binary and ternary phases need to be considered to further limit the region allowed by the chemical potential. Since Al, Ga, and N atoms may form GaN, AlN, $AlGaN_2$, Al_2GaN_3, and Al_3GaN_4 compounds, in order to avoid the formation of these competing phases, the chemical potential needs to satisfy the following conditions:

$$\Delta\mu_{Ga} + \Delta\mu_{N} \le \Delta H_f\left(GaN\right), \tag{3}$$

$$\Delta\mu_{Al} + \Delta\mu_{N} \le \Delta H_f\left(AlN\right), \tag{4}$$

$$\Delta\mu_{Al} + \Delta\mu_{Ga} + 2\Delta\mu_{N} \le \Delta H_f\left(AlGaN_2\right), \tag{5}$$

$$2\Delta\mu_{Al} + \Delta\mu_{Ga} + 3\Delta\mu_{N} \le \Delta H_f\left(Al_2GaN_3\right), \tag{6}$$

$$3\Delta\mu_{Al} + \Delta\mu_{Ga} + 4\Delta\mu_{N} \le \Delta H_f\left(Al_3GaN_4\right). \tag{7}$$

The allowable regions of $\Delta\mu_{Al}$ and $\Delta\mu_{Ga}$ can be determined based on Eqs. (3)–(7), as shown in Fig. 1 in the shaded part (quadrilateral EFGH), and the coordinates of several special points are listed in Table 1.

Table 1. Special point coordinates for constructing the stability region of the Al–Ga–N systems.

Position	$\Delta\mu_{Al}$ (eV)	$\Delta\mu_{Ga}$ (eV)	$\Delta\mu_{N}$ (eV)
A	0	0	−2.896
B	0	−4.344	0
C	−8.689	0	0
E	−6.504	−1.093	0
F	−6.694	−0.998	0
G	−5.696	0	−0.998
H	−5.411	0	−1.093

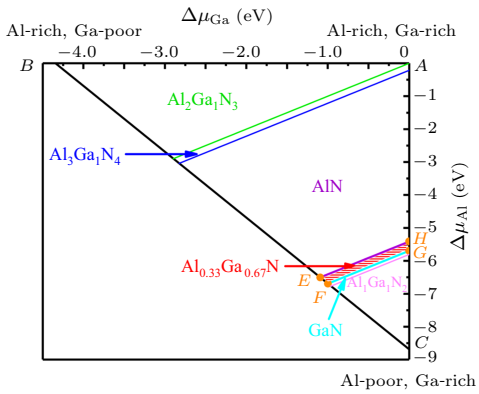


Fig. 1. The thermodynamic chemical potential stability region in $Al_{0.33}Ga_{0.67}N$ compound at ($\Delta\mu_{Al}$, $\Delta\mu_{Ga}$) plane. All the heat of formations for the compounds are from DFT calculated results. The red shaded area represents the stable range of the compound.

In addition, in order to prevent the formation of C defect-related competing compounds (AlC, AlC_3, Al_4C_3, GaC, GaC_3), it is required that

$$m\Delta\mu_{Al} + n\Delta\mu_{Ga} + p\Delta\mu_{C} \le \Delta H_f\left(Al_mGa_nC_p\right). \tag{8}$$

When simulating the growth environment of $Al_{0.33}Ga_{0.67}N$ crystal, we selected 4 representative points in the stable region of chemical potential and, combined with Eq. (8), obtained $\Delta\mu_C$ of *E*, *F*, *G*, and *H* points as −1.034, −1.129, −2.126, and −2.126 eV, respectively. The defect formation energies for C_{Al}, C_{Ga}, C_N substitutional defects, and C_i interstitial defect are finally obtained, as shown in Fig. 2. Considering that there are few Al atoms in this alloy system, for C_N defects, most of its nearest cations are Ga atoms, and only the configurations in which the nearest neighbors of the defects are Ga atoms (the lowest formation energy) are drawn in the figure. Other configurations will be further discussed in the subsequent work.

Figure 2 only displays the lowest energy charge states corresponding to C_{Al}, C_{Ga}, C_N, and C_i defect transition levels. The slopes of line segments correspond to different charge states, and the inflection points correspond to the transition energies of defects between different charge states. We found that the C_i defect formation energy is very high under these four chemical potential conditions, and only when the Fermi level is close to VBM (only under *G* and *H* chemical potential conditions), it is stable as C_i^{2+}. When the C atom occupies the cation site, its formation energy is also high. As shallow donor defects, C_{Ga} and C_{Al} exist stably in the +1 state only at *E*, *F* points with the low Fermi level, while at any other Fermi level they are not easy to occur. In addition, for the C_N defect with the lowest formation energy, it is the most stable structure when the Fermi level is greater than 1.86, 1.94, 0.87, and 0.75 eV, respectively, in *E*, *F*, *G*, and *H* points. Therefore, we predict that the C defect will occupy the N position in the n-type $Al_{0.33}Ga_{0.67}N$. The +/0 and 0/− transition levels are located at 0.62 eV and 1.11 eV above VBM, respectively, which is basically consistent with the defect behavior of C_N defect in GaN and AlN.[16–18] Our subsequent research will focus on the photoelectric properties related to C_N defects in $Al_xGa_{1-x}N$ alloys.

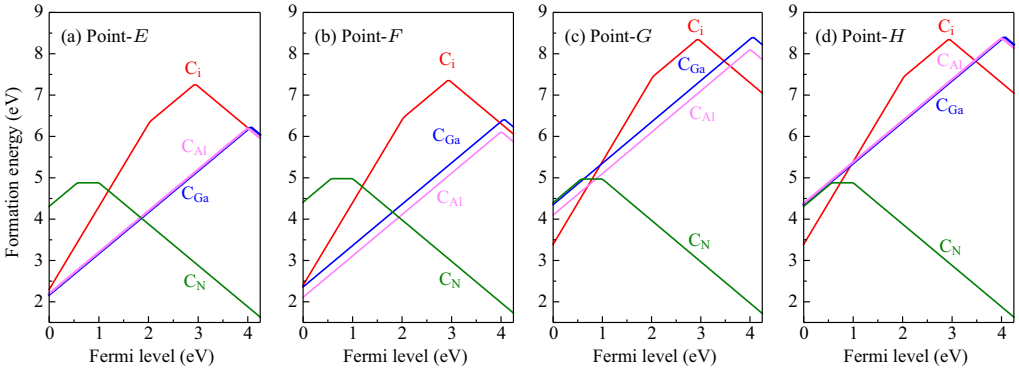


Fig. 2. Formation energies of C_{Al}, C_{Ga}, C_N substitutional, and C_i interstitial defects in $Al_{0.33}Ga_{0.67}N$ at different charge states *versus* Fermi level. The chemical potential environment at point (a) *E*, (b) *F*, (c) *G*, and (d) *H*.

3.2. C_N defect nearest neighbor cation arrangement in $Al_xGa_{1-x}N$ alloy

In order to investigate the properties of C_N defects, we simulated $Al_xGa_{1-x}N$ alloys with three different Al contents ($x = 0.33$, 0.50, and 0.61) using 128-atom supercells. Since the atom probe tomography found that the cations in most ternary nitride alloys were randomly distributed in the system,[24] for 0.33, 0.50, and 0.61 Al contents, we randomly replaced 21, 32, and 39 Al atoms at Ga sites, respectively. Considering the polar anisotropy along the [0001] crystallographic orientation and the arrangement of the nearest neighbor atoms around the C_N defect, we constructed 8 possible C_N defect configurations for each Al content, as shown in Fig. 3(a).

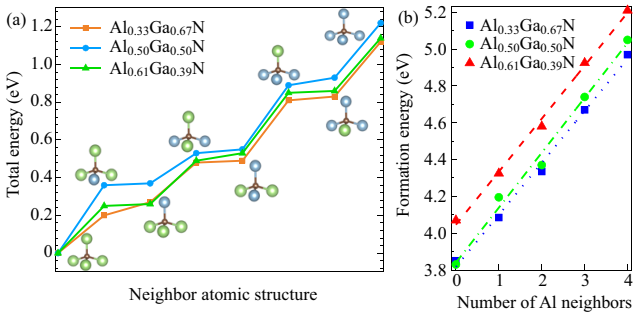


Fig. 3. (a) Total energies of the 8 possible C_N variants relative to the lowest energy configuration and (b) the formation energy of 5 possible defect configurations as a function of the number of Al neighbors ($n = 0$, 1, 2, 3, 4) in $Al_xGa_{1-x}N$ ($x = 0.33$, 0.50, 0.61). The illustrations correspond to the configurations of the nearest neighbor atoms, where the blue, green, and brown spheres represent Al, Ga, and C atoms, respectively.

We first conducted energetic stability analysis of eight defect configurations across varying Al compositions, as illustrated in Fig. 3(a). The C_N defect configuration with zero Al nearest neighbors (Ga-exclusive coordination environment) was selected as the reference system. When the number of Al neighbors (n) is the same, whether the Al atom is located in the polar direction has little effect on the total energies (less than 0.02 eV). The total energies of the systems increase with the number of Al neighbors. In addition, the total energy of the C_N defect system increases by 0.22 eV–0.36 eV for each additional neighbor Al atom. We changed the distribution of the next nearest neighbor atoms around the defects for any C_N defect configuration and found that the total energy of the system is almost unaffected, which further validates the rationality of our classification of the C_N defect configuration by the number of Al neighbors. Figure 3(b) shows the variation of defect formation energy with the number of Al neighbors ($n = 0$, 1, 2, 3, 4) in $Al_xGa_{1-x}N$ ($x = 0.33$, 0.50, 0.61). It is found that the formation energy increases almost linearly with n, which proves that in $Al_xGa_{1-x}N$ alloy, the formation energy is closely related to the number of Al atoms in the nearest neighbors of the defect,[37] and the formation energy of each configuration of each Al content differs by 1.12 eV–1.22 eV. Therefore, in the actual growth process of AlGaN alloy, these defect configurations may be formed.

3.3. Thermodynamic transition levels

The charge-state transition level between two charge states of a defect is given by the Fermi level position. The transition point between two charge states is found where the formation energies are equal. In the case of C_N, the transition level (+/0) is calculated as

$$\varepsilon(+/0) = \Delta H_f\left(C_N^+\right) - \Delta H_f\left(C_N^0\right) - E_{VBM}. \tag{9}$$

The sensitivity of the transition level to the nearest neighbor cation distribution in the alloy was studied by the above equation. As shown in Figs. 4(a)–4(c), we calculated the positions of the defect transition levels (red data in the figure) relative to VBM for 8 different C_N configurations, where the blue data represent their average values. For $Al_xGa_{1-x}N$ alloys with compositions $x = 0.33$, 0.50, and 0.61, the corresponding bandgap values measure 4.25 eV, 4.60 eV, and 4.93 eV, respectively. The energy differences among C_N transition levels across the eight configurations range from 0.10 eV to 0.18 eV. Figure 4(d) shows the variation trend of $Al_xGa_{1-x}N$ band edge and the average C_N transition level with Al content. It is concluded that the CBM increases faster than VBM with Al content, the average transition levels of C_N (+/0) and C_N (0/−)

shift slightly upward relative to VBM (consistent with other theoretical results[38]), and the band gap of the alloy increases from 3.52 eV ($x = 0$) to 6.03 eV ($x = 1$). The positions of these defect transition levels in the band gap will determine the photoluminescence energy involved in the defect and the non-radiative recombination rate of carriers.

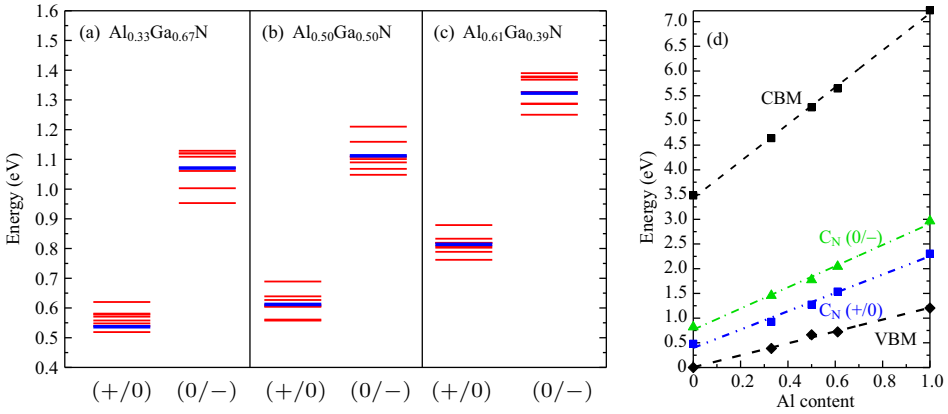


Fig. 4. Transition levels of C_N in (a) $Al_{0.33}Ga_{0.67}N$, (b) $Al_{0.5}Ga_{0.5}N$, (c) $Al_{0.61}Ga_{0.39}N$ for the 8 distinct atomic configurations (red lines), and the blue lines are the average values; (d) the position of the $Al_xGa_{1-x}N$ band edge and the average transition level as a function of the Al content.

3.4. Optical transition of C_N defect

As shown in Fig. 5(a), we use a dimensional configuration-coordinate diagram to illustrate the C_N defect-related optical transition process in AlGaN alloys, where the horizontal axis is the configuration-coordinate and the vertical axis is the total energy of the defect system. PA is an excited electron process from ground state to excited state ($C_N^0 \rightarrow C_N^+ + e^-$ and $C_N^- \rightarrow C_N^0 + e^-$), and PL is a de-excited process from excited state to ground state ($C_N^+ + e^- \rightarrow C_N^0$ and $C_N^0 + e^- \rightarrow C_N^-$). Based on first-principles, we calculated the PA and PL energies related to various C_N defect configurations in the alloy phase of different Al contents. Since the position of the defect transition level determines its optical transition energy, the transition level of the same content under different configurations ranges from 0.10 eV to 0.18 eV. As a result, the corresponding PA and PL energies fluctuate around 0.15 eV. Considering that the effect of Al content on optical transition energy is much greater than that of different configurations, we calculated the PA and PL energies associated with C_N defect as a function of the Al content in $n = 2$ defect configurations, as shown in Fig. 5(b). With the increase of Al contents in the alloy, the energy differences of C_N $(0/+)$ and C_N $(-/0)$ transition levels relative to CBM/VBM increase significantly, resulting in a blue shift trend in both PA and PL energies, with the energies changing linearly within the range of 1.51 eV to 2.07 eV. The PL peak of C_N $(0/+)$ extends from 2.62 eV to 4.2 eV, while the PA energy covers a band ranging from 3.32 eV to 5.39 eV. Additionally, the PL energy of C_N $(-/0)$ ranges from 2.16 eV to 3.67 eV, and the PA energy spans from 3.01 eV to 4.89 eV. This trend is highly consistent with the experimental data obtained through absorption spectroscopy and photoluminescence spectroscopy in references[20,38–42] in C-doped $Al_xGa_{1-x}N$ alloys. Specifically, within the composition range of $x = 0$ to 0.6, the deviation between the calculated and measured values is less than 3%. In conclusion, Al content can effectively regulate the wavelength range of C_N defects luminescence and absorption.

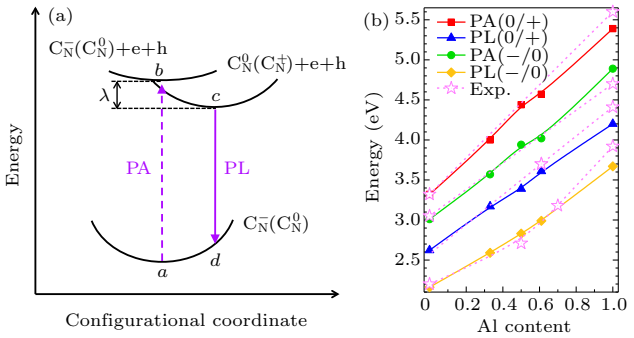


Fig. 5. (a) Configuration-coordinate diagram shows a series of optical transition processes for C_N defects in AlGaN alloys, and (b) the calculated PA and PL at the C_N $(0/+)$ and C_N $(-/0)$ transition levels as a function of the Al content. The stars ☆ are the PL experimental data[20,38–42] of C_N defect in AlGaN.

3.5. Non-radiative carrier recombination

In semiconductor optoelectronic devices, the recombination process of photogenerated carriers is the key physical process that determines the efficiency of the device. The internal quantum efficiency (IQE) can be expressed as IQE $= R_r/(R_r + R_{nr})$, where R_r is the radiative recombination rate, which is the process where electrons directly jump from the conduction band to the valence band and combine with holes, releasing energy in the form of emitted photons, which is an ideal energy conversion pathway; R_{nr} is the non-radiative recombination (non-RR) rate, which is the process where electron–hole pairs dissipate energy by emitting phonons or through the transfer of carrier kinetic energy during recombination, rather than emitting photons. This recombination process is typically described by the Shockley–Read–Hall (SRH)

model.[43,44] It is the main cause of device performance degradation and efficiency loss. Understanding and suppressing non-radiative recombination is a core issue for enhancing the performance of almost all photovoltaic devices.

The C_N deep acceptor center can capture holes from the valence band in the form of non-radiative recombination, and the rate is given by the following formula:

$$R_{ab} = \frac{1}{h}\left(\frac{\pi}{\lambda kT}\right)^{1/2}\left[kT\sum_l \frac{\left|\sum_i \langle a\left|\frac{\partial H}{\partial R_i}\right|b\rangle V_l(i)/\sqrt{m_i}\right|^2}{\omega_l^2}\right] \times \exp\left[-(\Delta E-\lambda)^2/4\lambda kT\right], \quad (10)$$

where a and b represent the initial and final electronic states. In our work, the initial state represents the defect level, and the final state represents the VBM. In our calculations, the VBM of undoped bulk GaN is doubly degenerate (as shown in Fig. S3), consistent with the degenerate heavy-hole and light-hole levels reported in Ref. [45]. The introduction of C_N defects will cause the previously doubly degenerate VBM energy levels to split (as shown in Fig. S3). For non-radiative capture calculations, the de-degenerated VBM is selected as the final state. $V_l(i)$ is the normalized phonon mode l vector with atom index i, ω_l is the phonon frequency, m_i is the nuclear mass, $\Delta E = E_a - E_b$ that E_a and E_b are the initial and final state energies, and reorganization energy λ is the atomic relaxation energy after electron state transition.

Then we use the combined dynamic matrix (CDM) method to calculate phonon patterns and density of states (DOS) at different Al contents. The result is shown in Fig. 6, where the black dashed line represents the DOS with perfect $Al_xGa_{1-x}N$ bulk. In AlGaN alloys, the phonon frequency can be described by the following formula

$$\omega \propto \sqrt{k/\mu}, \quad (11)$$

where k is the force constant of the bond and μ is the reduced mass. Since the mass of an Al atom is smaller than that of a Ga atom, leading to a shift of the phonon frequency toward higher frequencies as the Al composition increases. This shift has a significant impact on the subsequent carrier capture cross-section. The capture coefficient can be calculated by $C_p = R_{ab}\cdot V$ (V is volume of the supercell).[46] For the hole capture cross-section, the formula is $\sigma_p = C_p/v_p$, the average heat rate of hole is $v_p = (3k_BT/m_p)^{1/2}$, and the average hole effective mass m_p in $Al_xGa_{1-x}N$ varies linearly between 1.5 m_0 ($x=0$) and 5.4 m_0 ($x=1$),[47,48] and when Al content $x = 0.33, 0.50, 0.61$, m_p is taken as 2.7 m_0, 3.3 m_0, and 3.8 m_0 in this work, respectively.

When the defect center is charged, the Coulomb interaction between the carriers and the defect center significantly affects the capture rate. For the capture of holes by the negatively charged C_N defects in this study, the enhancement effect of the capture rate due to the Coulomb attractive potential must be considered. This effect is quantitatively corrected by the Sommerfeld factor for Coulomb corrections[49]

$$s(T) = \begin{cases} \frac{4}{\sqrt{\pi}}\left[\frac{Z^2\theta_b}{T}\right]^{1/2}, & Z<0, \\ \frac{8}{\sqrt{3}}\left[\frac{Z^2\theta_b}{T}\right]^{2/3}\exp\left(-3\left[\frac{Z^2\theta_b}{T}\right]^{1/3}\right), & Z>0, \end{cases} \quad (12)$$

where the characteristic temperature

$$\theta_b = m^* e^4/[32k_B(\varepsilon_r\varepsilon_0)^2\hbar^2]$$

is determined by the basic physical parameters of the material, m^* is the carrier effective mass, ε_r is the relative dielectric constant of the material, which is approximately 8.9 in $Al_xGa_{1-x}N$,[35,36] and Z is the charge of the Coulomb center (in units of the elementary charge e). We obtained the $s(T)$ of the $Al_xGa_{1-x}N$ alloy with x being 0.3, 0.5, and 0.61 were 30.01, 33.18, and 35.60 at 300 K, respectively (as shown in Fig. S4). And we reformulate the formula for non-radiative recombination rate as $C = s(T)\cdot\widetilde{C}$, where $\widetilde{C}$ is the capture coefficient calculated in a neutral defect-containing supercell.

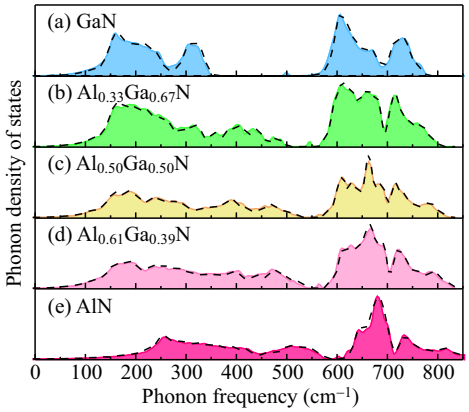


Fig. 6. Phonon density of states for C_N defect in (a) GaN, (b) $Al_{0.33}Ga_{0.67}N$, (c) $Al_{0.5}Ga_{0.5}N$, (d) $Al_{0.61}Ga_{0.39}N$, and (e) AlN. The black dashed line indicates $Al_xGa_{1-x}N$ phonon DOS without defects in the corresponding Al content.

As quantitatively demonstrated in Fig. 7, the hole capture cross-sections of C_N (0/+) and C_N (−/0) exhibit remarkable configuration-dependent variations at 300 K, with double arrows indicating the transition energy ranges for different local environments at fixed Al compositions. In both Figs. 7(a) and 7(b), the capture cross-sections of all three $Al_xGa_{1-x}N$ compositions exhibit a decreasing trend with increasing transition energy. Specifically, Fig. 7(a) (for 0/+ transition) shows the ordinate spanning 10^{-14} cm^2 to 10^{-12} cm^2 as the abscissa rises from 0.5 eV to 0.9 eV, while Fig. 7(b) (for 0/− transition) has the ordinate ranging from 10^{-20} cm^2 to 10^{-13} cm^2 with the abscissa increasing from 0.8 eV to 1.4 eV. Our analysis of the non-RR coefficient in Eq. (10) reveals a critical insight: while the reorganization energy λ remains configuration-insensitive,

the transition energy ΔE dominates the σ_p variations — establishing ΔE as the primary tuning knob for carrier capture processes (see Table 2 for complete parameter ranges). Specifically, a 0.1-eV fluctuation in the defect transition energy induced by configuration leads to an order-of-magnitude variation in the carrier capture cross-section. This work advances beyond conventional defect studies by elucidating three fundamental principles for ternary alloys: (i) Configuration effects follow quantifiable scaling laws. (ii) Al content increase universally suppresses capture cross-sections of C_N defect center. (iii) The ΔE–σ_p correlation holds across different charge states. Although C_N defects in AlGaN are always detrimental, under high Al conditions, their ability to capture carriers has weakened. In areas where C_N defects are inevitable, we can adopt some strategies to increase the Al content as much as possible to mitigate their negative effects, or through band engineering, confine the carriers to high-quality, low-defect regions, so that they have no chance to come into contact with any type of recombination center, thereby reducing the light energy loss caused by non-radiative recombination and improving the luminous efficiency. Notably, our findings contrast with traditional binary semiconductors where defect properties are typically composition-independent. The dual control mechanism (configuration tuning plus cationic content adjustment) demonstrated here provides a blueprint for defect engineering in emerging quaternary alloys like AlInGaN. For device applications, these principles enable precise customization of carrier lifetimes — particularly valuable for UV photodetectors requiring controlled recombination kinetics. Future studies could extend this framework to other defect types, potentially establishing a unified theory for defect behavior in compositionally complex semiconductors.

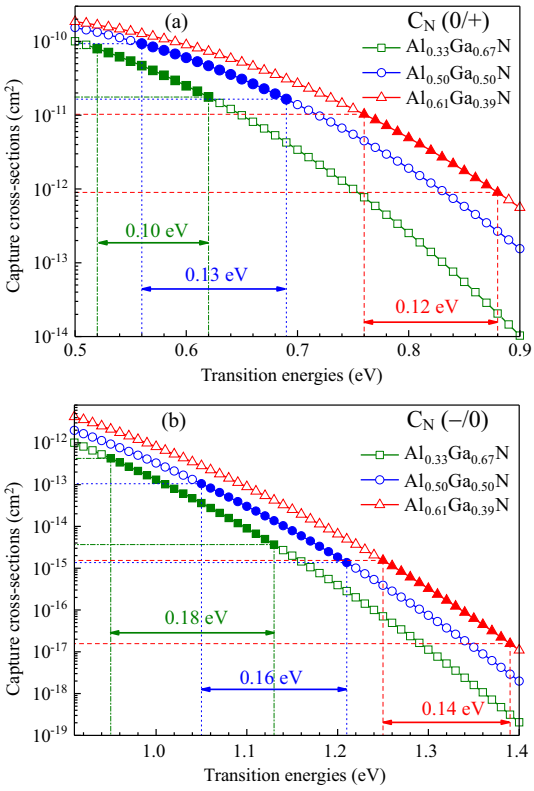


Fig. 7. Transition energies-dependent hole capture cross-section of (a) C_N (0/+) and (b) C_N (−/0) transition levels in $Al_xGa_{1-x}N$ ($x = 0.33$, 0.50, 0.61) at 300 K. The solid data points represent the hole capture cross-sections corresponding to the transition level variation range.

Table 2. Transition energy ΔE, non-radiative recombination rate R_{ab}, coefficient C_p and hole capture cross-section σ_p corresponding to the 0/+ and −/0 transition levels of C_N defect in $Al_xGa_{1-x}N$.

Level	x	ΔE (eV)	R_{ab} (s^{-1})	C_p ($cm^3 \cdot s^{-1}$)	σ_p (cm^2)
0/+	0.33	0.52–0.62	3.78×10^{17}–8.34×10^{16}	4.98×10^{-4}–1.10×10^{-4}	7.99×10^{-11}–1.76×10^{-11}
	0.50	0.56–0.69	4.41×10^{17}–7.80×10^{16}	5.81×10^{-4}–1.03×10^{-4}	9.32×10^{-11}–1.65×10^{-11}
	0.61	0.76–0.88	4.88×10^{16}–4.27×10^{15}	6.41×10^{-5}–5.62×10^{-6}	1.03×10^{-11}–9.00×10^{-12}
−/0	0.33	0.95–1.13	2.00×10^{15}–1.74×10^{13}	2.64×10^{-6}–2.29×10^{-8}	4.24×10^{-13}–3.67×10^{-15}
	0.50	1.05–1.21	4.98×10^{14}–6.44×10^{12}	6.54×10^{-7}–8.49×10^{-9}	1.05×10^{-13}–1.36×10^{-15}
	0.61	1.25–1.39	7.26×10^{12}–7.33×10^{10}	9.58×10^{-9}– 9.75×10^{-11}	1.53×10^{-15}–1.56×10^{-17}

4. Conclusion

In summary, our first-principles calculations with the HSE06 hybrid functional reveal unprecedented configuration-dependent characteristics of C_N defects in wurtzite $Al_xGa_{1-x}N$ alloys. The defect formation energy exhibits remarkable sensitivity to local cation environments, following an almost perfect linear scaling with Al neighbor count ($n = 0$–4). Notably, the energy difference between extreme configurations ($n = 0$ *versus* $n = 4$) reaches 1.12 eV–1.22 eV, explaining the coexistence of multiple defect states in as-grown alloys. More importantly, we discover a unified linear scaling law governing three key optoelectronic parameters: (i) defect transition levels, (ii) PA/PL energies, and (iii) non-radiative recombination rates, all precisely tunable via Al content modulation. This quantitative framework establishes $Al_xGa_{1-x}N$ as a model system for defect engineering, where simple composition control enables predictable adjustment of emission spectra and carrier dynamics–a breakthrough for developing wavelength-programmable UV optoelectronic devices.

Acknowledgements

Project supported by the National Natural Science Foundation of China (Grant Nos. 12004204, 11964022, and 12274360), the Natural Science Foundation of Inner Mongo-

lia Autonomous Region of China (Grant Nos. 2023ZD27 and 2024MS01010), the Science and Technology Plan Projects of Inner Mongolia Autonomous Region of China (Grant No. 2023KYPT0012), and the GHfund B (Grant No. ghfund202407028086).

References

[1] Kneissl M, Kolbe T, Chua C, Kueller V, Lobo N, Stellmach J, Knauer A, Rodriguez H, Einfeldt S, Yang Z, Johnson N M and Weyers M 2010 *Semicond. Sci. Technol.* **26** 014036

[2] Jones K A, Chow T P, Wraback M, Shatalov M, Sitar Z, Shahedipour F, Udwary K and Tompa G S 2015 *J. Mater. Sci.* **50** 3267

[3] Fan F H, Syu Z Y, Wu C J, Yang Z J, Huang B S, Wang G J, Lin Y S, Chen H, Hauer Kao C and Lin C-F 2017 *Sci. Rep.* **7** 4968

[4] Dinh D V, Hu N, Honda Y, Amano H and Pristovsek M 2018 *J. Cryst. Growth* **498** 377

[5] Irmscher K, Hartmann C, Guguschev C, Pietsch M, Wollweber J and Bickermann M 2013 *J. Appl. Phys.* **114** 123505

[6] Alden D, Harris J S, Bryan Z, Baker J N, Reddy P, Mita S, Callsen G, Hoffmann A, Irving D L, Collazo R and Sitar Z 2018 *Phys. Rev. Appl.* **9** 054036

[7] Irmscher K, Gamov I, Nowak E, Gärtner G, Zimmermann F, Beyer F C, Richter E, Weyers M and Tränkle G 2018 *Appl. Phys. Lett.* **113** 262101

[8] Gamov I, Hartmann C, Wollweber J, Dittmar A, Straubinger T, Bickermann M, Kogut I, Fritze H and Irmscher K 2019 *J. Appl. Phys.* **126** 215102

[9] Tillner N, Frankerl C, Nippert F, Davies M J, Brandl C, Lösing R, Mandl M, Lugauer H J, Zeisel R, Hoffmann A, Waag A and Hoffmann M P 2020 *Phys. Status Solidi B* **257** 2000278

[10] Zimmermann F, Beyer J, Beyer F C, Gärtner G, Gamov I, Irmscher K, Richter E, Weyers M and Heitmann J 2021 *J. Appl. Phys.* **130** 055703

[11] Kojima K, Horikiri F, Narita Y, Yoshida T, Fujikura H and Chichibu S F 2019 *Appl. Phys. Express* **13** 012004

[12] Chichibu S F, Kojima K, Hazu K, Ishikawa Y, Furusawa K, Mita S, Collazo R, Sitar Z and Uedono A 2019 *Appl. Phys. Lett.* **115** 151903

[13] Wickramaratne D, Dreyer C E, Shen J X, Lyons J L, Alkauskas A and Van De Walle C G 2020 *Phys. Status Solidi B* **257** 1900534

[14] Zang H, Sun X, Jiang K, Chen Y, Zhang S, Ben J, Jia Y, Wu T, Shi Z and Li D 2021 *Adv. Sci.* **8** 2100100

[15] Chahshouri F, Taleb M, Black M, Mensing M and Talebi N 2024 *J. Phys. Appl. Phys.* **57** 465104

[16] Lyons J L, Janotti A and Van de Walle C G 2014 *Phys. Rev. B* **89** 035204

[17] Gordon L, Lyons J L, Janotti A and Van de Walle C G 2014 *Phys. Rev. B* **89** 085204

[18] Wu S, Yang X, Zhang H, Shi L, Zhang Q, Shang Q, Qi Z, Xu Y, Zhang J, Tang N, Wang X, Ge W, Xu K and Shen B 2018 *Phys. Rev. Lett.* **121** 145505

[19] Collazo R, Xie J, Gaddy B E, Bryan Z, Kirste R, Hoffmann M, Dalmau R, Moody B, Kumagai Y, Nagashima T, Kubota Y, Kinoshita T, Koukitu A, Irving D L and Sitar Z 2012 *Appl. Phys. Lett.* **100** 191914

[20] Demchenko D O, Diallo I C and Reshchikov M A 2013 *Phys. Rev. Lett.* **110** 087404

[21] Gaddy B E, Bryan Z, Bryan I, Xie J, Dalmau R, Moody B, Kumagai Y, Nagashima T, Kubota Y, Kinoshita T, Koukitu A, Kirste R, Sitar Z, Collazo R and Irving D L 2014 *Appl. Phys. Lett.* **104** 202106

[22] Reshchikov M A, Demchenko D O, Usikov A, Helava H and Makarov Yu 2014 *Phys. Rev. B* **90** 235203

[23] Zhang H S, Shi L, Yang X B, Zhao Y J, Xu K and Wang L W 2017 *Adv. Opt. Mater.* **5** 1700404

[24] Rigutti L, Bonef B, Speck J, Tang F and Oliver R A 2018 *Scr. Mater.* **148** 75

[25] Reshchikov M A and Morkoç H 2005 *J. Appl. Phys.* **97** 061301

[26] Alkauskas A, Lyons J L, Steiauf D and Van de Walle C G 2012 *Phys. Rev. Lett.* **109** 267401

[27] Henry C H and Lang D V 1997 *Phys. Rev. B* **15** 989

[28] Alkauskas A, Yan Q and Van de Walle C G 2014 *Phys. Rev. B* **90** 075202

[29] Wickramaratne D, Shen J X, Dreyer C E, Engel M, Marsman M, Kresse G, Marcinkevičius S, Alkauskas A and Van De Walle C G 2016 *Appl. Phys. Lett.* **109** 162107

[30] Heyd J, Scuseria G E and Ernzerhof M 2003 *J. Chem. Phys.* **118** 8207

[31] Heyd J, Scuseria G E and Ernzerhof M 2006 *J. Chem. Phys.* **124** 219906

[32] Jia W, Fu J, Cao Z, Wang L, Chi X, Gao W and Wang L 2013 *J. Comput. Phys.* **251** 102

[33] Jia W, Cao Z, Wang L, Fu J, Chi X, Gao W and Wang L 2013 *Comput. Phys. Commun.* **184** 9

[34] Wei S H and Zunger A 1995 *J. Appl. Phys.* **78** 3846

[35] Darakchieva V, Monemar B and Usui A 2007 *Appl. Phys. Lett.* **91** 031911

[36] Madelung O 1996 *Semiconductors-basic data* (Berlin, Heidelberg: Springer)

[37] Bogusławski P and Bernholc J 1999 *Phys. Rev. B* **59** 1567

[38] Reddy P, Bryan Z, Bryan I, Kim J H, Washiyama S, Kirste R, Mita S, Tweedie J, Irving D L, Sitar Z and Collazo R 2020 *Appl. Phys. Lett.* **116** 032102

[39] Bickermann M, Epelbaum B M and Winnacker A 2004 *J. Cryst. Growth* **269** 432

[40] Shen Y, Zhang X, Fan A, Chen B, Tian Y, Luo X, Lyu J, Lai M J, Hu G and Cui Y 2022 *Mater. Sci. Semicond. Process.* **151** 107002

[41] Singh R, Roy A and Rao C N R 2022 *ACS Appl. Electron. Mater.* **4** 3147

[42] Hyun Kim J, Bagheri P, Kirste R, Reddy P, Collazo R and Sitar Z 2023 *Phys. Status Solidi A* **220** 2200390

[43] Shockley W and Read W T 1952 *Phys. Rev.* **87** 835

[44] Hall R N 1952 *Phys. Rev.* **87** 387

[45] Vurgaftman I, Meyer J R and Ram-Mohan L R 2001 *J. Appl. Phys.* **89** 5815

[46] Nelson J 2003 *The Physics of Solar Cells* (United Kingdom: Imperial College Press)

[47] Kim K, Lambrecht W R L, Segall B and van Schilfgaarde M 1997 *Phys. Rev. B* **56** 7363

[48] Tian A, Liu J, Ikeda M, Zhang S, Li Z, Feng M, Zhou K, Li D, Zhang L, Wen P, Zhang F and Yang H 2015 *Appl. Phys. Express* **8** 051001

[49] Turiansky M E, Alkauskas A and Van De Walle C G 2024 *J. Phys. Condens. Matter* **36** 195902